RSC Sustainability

ROYAL SOCIETY OF CHEMISTRY

PAPER

View Article Online
View Journal | View Issue

Cite this: *RSC Sustainability*, 2023, **1**, 1278

Sustainable utilization of natural sands for cleaner preparation of high-performance nanostructured cobalt blue composite pigments by dolomite-induced mechanochemistry†

Hao Yang,[ab] Bin Mu, *[ab] Tenghe Zhang,[ab] Yushen Lu[a] and Aiqin Wang *[ab]

The strategic concept of green and sustainable development has given birth to a series of technologies for cleaner conversion and value-added utilization of natural mineral resources. In this study, a cleaner route of dolomite ($CaMg(CO_3)_2$)-induced mechanochemical preparation of cobalt blue composite pigments with lower cobalt consumption and high blue intensity derived from the abundant natural sands (sea sand and desert sand) was developed. The characterization results revealed that mechanical forces realized the ingenious activation of natural sands and dolomite. The activated natural sands provided the silicon source for the formation of anorthite ($CaAl_2Si_2O_8$) to improve the lightness of the composite pigments. The Ca and Mg species derived from dolomite transformed into $CaAl_2O_4$ and $MgAl_2O_4$ accompanied by the formation of $CoAl_2O_4$, which was favorable for the distortion of the crystal structure of $CoAl_2O_4$ and the improvement of reflectance to blue light. The lamellar dolomite served as a benign substrate to induce the formation of $CoAl_2O_4$ nanoparticles on its surface and improve the dispersion. The as-prepared composite pigments exhibited more excellent color performances than those of the commercial and house-made pure cobalt blue pigments due to the above-mentioned synergistic effect, and the b^* value of cobalt blue composite pigments prepared with sea sand reached −50.30. In addition, composite pigments exhibited excellent environmental stability and high temperature resistance to be applied as promising outdoor coatings. Therefore, this study is expected to provide a cleaner strategy for the construction of high-performance cobalt blue pigments with low cobalt content and high blue intensity, as well as direct value-added and sustainable utilization of huge amounts of natural sands.

Received 24th December 2022
Accepted 18th June 2023

DOI: 10.1039/d2su00146b

rsc.li/rscsus

Sustainability spotlight

At present, $CoAl_2O_4$ pigments are still irreplaceable among commercial inorganic and organic blue pigments, but their relevant applications are severely restricted due to the high cost of cobalt sources and preparation technique defects, especially the high calcination temperature of the solid-phase method, and large amounts of waste liquids discharged from the liquid-phase method. Therefore, a cleaner dolomite-induced mechanochemical method was developed to fabricate low-cost $CoAl_2O_4$ composite pigments combining natural sea sand or desert sand without discharging waste liquids in this study. It realized the cleaner production of $CoAl_2O_4$ pigments with high blue intensity and low cobalt consumption and the sustainable value-added utilization of dolomite and natural sands. Moreover, this study is aligned with the UN's Sustainable Development Goal 12 and 14.

1 Introduction

In recent years, the proposal of the advanced idea of green and sustainable development has attracted great attention from the scientific community and increasingly gained widespread acceptance.[1] For making a chemical transformation or material synthesis system greener and more sustainable, a series of strategies were developed taking into consideration the resources, wastes, hazards, and costs.[2–4] Among them, the emerging mechanochemistry has been explosively concerned and widely developed to fabricate various functional materials and induce chemical synthesis,[5–7] which initiates or sustains physical and chemical transformations *via* mechanical forces to

[a]*Key Laboratory of Clay Mineral Applied Research of Gansu Province, Center of Eco-material and Green Chemistry, Lanzhou Institute of Chemical Physics, Chinese Academy of Sciences, Lanzhou 730000, P. R. China. E-mail: mubin@licp.cas.cn*

[b]*Center of Materials Science and Optoelectronics Engineering, University of Chinese Academy of Sciences, Beijing 100049, P. R. China*

† Electronic supplementary information (ESI) available: Digital images (Fig. S1) and chemical composition (Table S1) of natural sands; XRD patterns of natural sands (Fig. S2) and dolomite (Fig. S3); XPS fine spectra of Ca 2p and Mg 1s of dolomite (Fig. S4); chemical composition of dolomite (Table S2); comparison of chroma parameters with other reports (Table S3); binding energy location and corresponding assignment (Table S4). See DOI: https://doi.org/10.1039/d2su00146b

offer a cleaner and eco-friendly strategy for the preparation of functional materials avoiding the usage and discharge of a large volume of solvents.[8] Thus, the developed mechanochemistry is expected to largely reduce the generation of wastes and hazards during reactions. Interestingly, the introduction of a small amount of liquid (*e.g.*, H_2O) can accelerate or even promote the chemical reaction to obtain products with higher crystallinity.[9] Furthermore, the mechanochemistry presents good sustainability and green chemistry metrics according to the numerical quantization of the "greenness" and calculation of energy consumption.[10–12] However, the sustainable development further requires us to rationally exploit and utilize mineral resources on the basis of green chemistry, especially the natural non-metallic mineral resources such as the tremendous clay minerals and natural sands (sea sand and desert sand, which are mainly composed of quartz). Therefore, it is crucial to realize the sustainable utilization of natural non-metallic mineral resources for environmental-friendly construction of high-performance functional materials combined with the mechanochemistry technology.

Among the blue inorganic pigments, spinel cobalt blue ($CoAl_2O_4$) was used as a mainstream and irreplaceable commercial inorganic blue pigment over the past two centuries by virtue of the strong covering ability and outstanding weather resistance since it was invented in 1802.[13,14] With the emergence and development of clean energy technologies, the strategic position of cobalt is increasingly significant because of the scarcity and low recovery ratio of cobalt resources.[15] Naturally, the production cost of $CoAl_2O_4$ is obviously increased in recent decades.[16] At present, substrate-type and doping-type $CoAl_2O_4$ pigments are developed for minimizing the cobalt consumption combined with the relevant preparation technologies. In the case of the substrate-type $CoAl_2O_4$ pigments, the incorporation of inorganic substrates could effectively induce $CoAl_2O_4$ nanoparticles to grow on the surface of inorganic substrates and prevent the agglomeration of pigment nanoparticles, which obviously reduced the production cost of $CoAl_2O_4$ pigments and simultaneously retained the excellent color performance.[16–19] Different from the former, the doping of metal ions (Mg^{2+}, Zn^{2+}, *etc.*) not only reduced the added amount of cobalt sources, but also affect the transitions of four-coordinated Co^{2+} to regulate the blue intensity of $CoAl_2O_4$ pigments by distorting the crystal structure.[14,20–22] Especially, Mg^{2+} can enter into the tetrahedral sites of spinel $CoAl_2O_4$ and form a solid solution with $CoAl_2O_4$, while the pigments were composed of the mixed phases of $CaAl_2O_4$ and $CoAl_2O_4$ after the incorporation of Ca^{2+} due to the difference in the ionic radius and coordination numbers between the introduced metal ions and Co^{2+}.[20,21]

However, the relevant liquid-phase preparation routes unavoidably involved the use of a large volume of solution, strong alkaline or organic reagents, and the discharge of waste liquid with a low yield. In our previous study, commercial synthetic heavy $CaCO_3$ was developed for the assisted preparation of $CoAl_2O_4$ composite pigments by a mechanochemical method in the presence of natural sea sand and desert sand.[23,24] However, it neglected the effect of Ca^{2+} derived from $CaCO_3$ on the color properties of $CoAl_2O_4$ composite pigments, and most of them were removed by water after being transferred from a grinding jar. As a typical Ca- and Mg-bearing carbonate mineral, dolomite ($CaMg(CO_3)_2$) is widely distributed in sedimentary rocks on the Earth, including continental lacustrine and marine settings.[25] It is worth noting that dolomite has been employed as an excellent natural Ca and Mg source to fabricate Ca–Mg–Al layered double hydroxides (LDHs),[25] Mg–Al–CO_3 LDHs,[26] and mesoporous calcium-magnesium silicate.[27] In addition, it was reported that dolomite with special stacked lamellar morphology could also be used as a substrate to support metal catalysts and improve the catalytic efficiency.[28,29] As far as we know, it was scarcely reported that a functional substrate with two roles of loading and doping was employed to fabricate high-performance $CoAl_2O_4$ pigments combined with the advantages of the incorporation of substrates or doping ions. Therefore, it is of great significance to investigate the feasibility of using dolomite as the source of Ca^{2+} and Mg^{2+} to regulate the blue intensity, and the substrate to *in situ* anchor $CoAl_2O_4$ nanoparticles with the assistance of the cleaner and sustainable mechanochemistry strategy, which contributed to reducing the usage of the synthesized chemical reagents and the consumption of cobalt source for the design of low-cost and high-performance $CoAl_2O_4$ pigments.

In this study, high-chroma $CoAl_2O_4$ composite pigments were facilely fabricated by a one-pot dolomite-induced mechanochemical method followed by a high-temperature crystallization process using sea sand or desert sand, Co_3O_4 and $Al(NO_3)_3\cdot 9H_2O$ as the raw materials (Scheme 1). During mechanical grinding, sea sand or desert sand was used as the grinding media, the crystal water of $Al(NO_3)_3\cdot 9H_2O$ was employed as a micro-liquid, and free Ca^{2+} and Mg^{2+} were generated by the neutralization reaction between dolomite and residual acid of $Al(NO_3)_3\cdot 9H_2O$. The phase composition, structural and morphological changes of the as-prepared precursor and composite pigments were characterized by X-ray diffraction (XRD), Fourier-transform infrared (FTIR) spectroscopy and transmission electron microscopy (TEM), while the phase transformation of the samples during the calcination process was studied by a synchronous thermal analysis combining

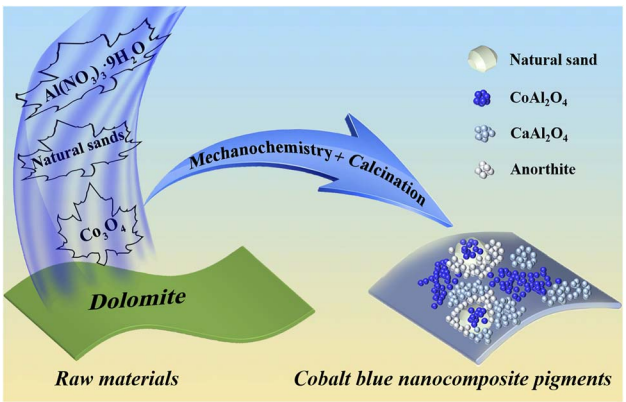

Scheme 1 Schematic diagram of the preparation process of $CoAl_2O_4$ composite pigments by a dolomite-induced mechanochemical method.

thermogravimetric analysis with differential thermal analysis (TG-DTA). Furthermore, X-ray photoelectron spectroscopy (XPS) was used to probe the possible interaction between the involved substrates and $CoAl_2O_4$ nanoparticles. Therefore, this study was expected to provide a cleaner strategy for the preparation of high-performance cobalt blue composite pigments with lower cobalt consumption.

2 Experimental section

2.1 Materials and instrument

Natural dolomite was obtained from the dolomite mine in Luxi County (Pingxiang, Jiangxi, China), and it was physically crushed followed by the process of filtering through a 400 mesh sieve before use. The chemical compositions were determined by X-ray fluorescence (XRF), and the main compositions were CaO and MgO (Table S1, ESI†). Co_3O_4 was provided by Zhongqin Chemical Reagent Co., Ltd. (Shanghai, China). $Al(NO_3)_3 \cdot 9H_2O$ was obtained from Xilong Scientific Co., Ltd. (Shantou, Guangdong, China). Sea sand was collected from Zhangpu County (ZPS, Fujian, China), while desert sand was obtained from a large wind zone in Hami (HMS, Xinjiang, China), and both of them were physically crushed to 200 mesh before use. A mini planetary high-energy ball mill was purchased from Fritsch GmbH (Germany), where the inner wall of the grinding bowl (45 mL in volume) and grinding ball (2 mm in diameter) were ZrO_2.

2.2 Preparation of $CoAl_2O_4$ composite pigments

Co_3O_4 (0.2408 g), dolomite (0.7498 g), $Al(NO_3)_3 \cdot 9H_2O$ (8.2529 g), 0.6368 g of ZPS (or HMS) and zirconia balls were put together into a 45 mL grinding pot, and the mass ratio of ball to materials was 10 : 1. Then, the mixes were ground at a speed of 500 rpm for 6 h. After the grinding process, the obtained precursors were directly calcined at 1100 °C for 2 h at a heating rate of 10 °C min^{-1} in a muffle furnace. The obtained precursors were labeled as Pre-D/CB/ZPS and Pre-D/CB/HMS and the corresponding composite pigments as CP-D/CB/ZPS and CP-D/CB/HMS, respectively. Moreover, the control samples without addition of dolomite or Co_3O_4 were also prepared and labeled as CP-CB/ZPS, CP-D/ZPS, CP-CB/HMS and CP-D/HMS, respectively.

2.3 Effect of acid treatment of natural sands on the color performance of composite pigments

Generally, natural sands presented different degrees of colors due to the existence of chromogenic species (*e.g.* Fe), which might bring negative or positive effects on the color performance of $CoAl_2O_4$ in the calcination process.[30] In order to investigate the effect of iron ions in natural sands on the color performance of the composite pigments, the involved natural sands were treated with a HCl solution. Typically, 20 g of ZPS or HMS were put in 50 mL of HCl (6 mol L^{-1}) followed by magnetic stirring for 12 h, and then the solid products were separated by centrifugation, washed using deionized water to neutral and dried in an oven at 60 °C before use. The resulting samples were named ZPS-A and HMS-A, respectively. Similarly, the obtained precursors were labelled as Pre-D/CB/ZPS-A and Pre-D/CB/HMS-A and the corresponding composite pigments as CP-D/CB/ZPS-A and CP-D/CB/HMS-A, respectively. The control samples without addition of dolomite or Co_3O_4 were also prepared and marked as CP-CB/ZPS-A, CP-D/ZPS-A, CP-CB/HMS-A and CP-D/HMS-A, respectively.

2.4 Evaluation of environmental stability

First, 1 g of the obtained composite pigments (CP-D/CB/ZPS-A and CP-D/CB/HMS-A) were dispersed evenly in 50 mL of HCl (1 mol L^{-1}), NaOH (1 mol L^{-1}) and ethanol solutions under continuous shaking for 24 h at a speed of 150 rpm on a shaker, and then, the solid samples were centrifuged, washed with deionized water to neutral and dried in an oven at 60 °C. The changes in the chroma values of composite pigments before and after exposure to different chemical environments were compared to evaluate their environmental stability.

2.5 Characterization techniques

The chroma parameters and reflectance spectra of the as-prepared composite pigments were collected using a Color-Eye automatic differential colorimeter (X-Rite, Ci 7800, USA) adopting the Commission Internationale de l'Eclairage (CIE) 1976 $L^*a^*b^*$ colorimetric method. The infrared spectra of the samples were recorded using a Thermo Nicolet 6700 FTIR spectrometer (Thermo Fisher Scientific, USA) in the wavenumber range of 400–4000 cm^{-1}. The XRD patterns of the samples were acquired with the working parameter of Cu Kα (λ = 1.54060 Å) using a SmartLab SE multifunctional X-ray diffractometer (Rigaku Co., Japan). TG-DTA curves of the samples were obtained using a STA 6000 (PerkinElmer Instrument Co., Ltd. USA) from room temperature to 1000 °C. X-ray photoelectron spectroscopy (XPS) characterization was carried out using an XSAM 800 instrument (Kratos Co., Ltd.). The micromorphology of composite pigments was observed using a JEM-2100 transmission electron microscope (TEM, JEOL, Ltd., Japan).

3 Results and discussion

3.1 Color performance of composite pigments

In the absence of chromogenic cobalt species (Co_3O_4), Pre-D/ZPS and Pre-D/HMS as well as CP-D/ZPS and CP-D/HMS presented white color (Fig. 1a). After the incorporation of Co_3O_4, the color of precursors turned into dark black under the mechanical force, and the obtained composite pigments possessed different degrees of blue. Interestingly, CP-D/CB presented poor color performance in the absence of ZPS and HMS, while the color performance of composite pigments (CP-CB/ZPS and CP-CB/HMS) was greatly enhanced with the introduction of ZPS and HMS. By contrast, the color performance of CP-D/CB/ZPS and CP-D/CB/HMS was further improved after the incorporation of dolomite. Moreover, the color performance of the prepared composite pigments based on pre-treated ZPS and HMS was superior, wherein the b^* values of CP-D/CB/ZPS-A and CP-D/CB/HMS-A reached −50.30 and −49.60 (Fig. 1c),

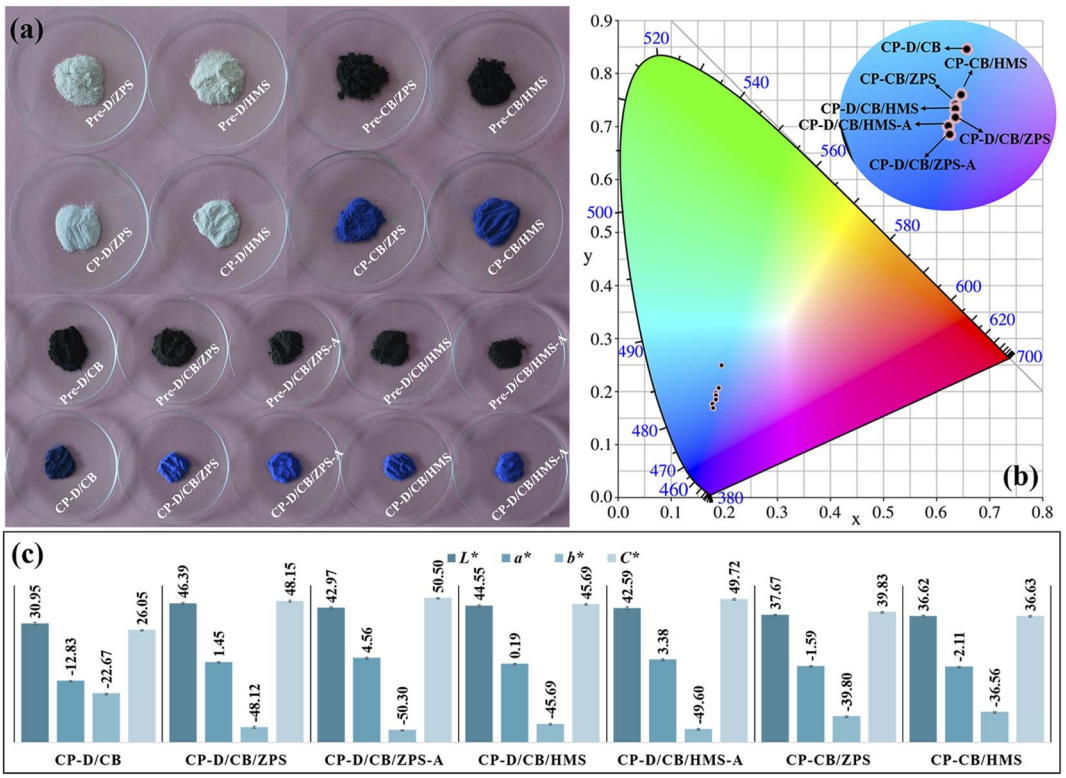

Fig. 1 (a) Digital photos of precursors and corresponding composite pigments, (b) chromaticity diagram and (c) chroma values of composite pigments.

respectively. The change trend of the color performance of the composite pigments was also consistent with the chromaticity diagram (Fig. 1b).

Due to the different geological causes, the content and existing states of iron compounds in natural sands were different, which were significant factors for the coloring degree of natural sands. The iron element generally existed in quartz in the form of dissolved salts in fluid inclusions or single-phase minerals (solid inclusions). Moreover, the iron element could also enter into the quartz lattice (substitutional and interstitial types). It was said that the third form was much hard to be removed compared with the first two forms, even when treated with hydrochloric and perchloric acids.[31] Obviously, their whiteness was greatly enhanced after acid treatment (Fig. S1, ESI†), and the chemical compositions of ZPS and HMS before and after acid treatment were characterized (Table S2, ESI†). The main chemical compositions of ZPS were SiO_2 and small amounts of K_2O and Fe_2O_3. Compared with ZPS, the SiO_2 and K_2O contents had no obvious change after acid treatment, while a small amount of iron element was removed in ZPS-A. In the case of HMS-A, the content of magnesium and iron elements decreased, and other components of SiO_2, Al_2O_3, Na_2O and K_2O had no visible changes compared with HMS. Thus, the improved whiteness of natural sands was related to the removal of Fe species. During the grinding process, the size of natural sands was greatly reduced, and thus iron compounds could be easily removed when iron existed in the form of a dissolved salt or a single-phase mineral.[32] After the high-temperature crystallization process, Fe^{3+} could occupy the octahedral Al^{3+} sites in $CoAl_2O_4$ due to the similar six-coordinated ionic radii, which brought about the negative effects on the color performance of $CoAl_2O_4$ due to the formation of black ferrate.[33] After HCl pretreatment of ZPS and HMS, Fe^{3+} was partly removed, and their whiteness was enhanced. Thus, CP-D/CB/ZPS-A and CP-D/CB/HMS-A exhibited better color performance than that of CP-D/CB/ZPS and CP-D/CB/HMS, respectively. In addition, residual Fe^{3+} was still confined in the quartz lattice after acid treatment, and the color performance of composite pigments was affected by the color of quartz. Therefore, CP-D/CB/ZPS-A presented a superior blueness hue to CP-D/CB/HMS-A because the iron content of HMS-A was higher than that of HMS-A (Table S2, ESI†).

In addition, the blue intensity of composite pigments prepared using original ZPS and HMS was already better than that of other reported pigments prepared at the same calcination temperature (Table S3, ESI†) as well as the commercial and house-made cobalt blue pigments, but the composite pigments presented lower cobalt consumption.[14,16,34–37] Thus, it could be concluded that it was feasible to construct $CoAl_2O_4$ composite pigments with low cobalt consumption and high blue intensity based on dolomite and natural sands with the assistance of mechanical forces, and the excellent color performance may be related to the introduction of dolomite and natural sands.

3.2 XRD patterns

From the XRD patterns of natural sands (Fig. S2, ESI†), it can be found that the main crystalline phases were quartz and feldspar in HMS, while there was only quartz in ZPS. Furthermore, only the characteristic diffraction peaks of dolomite were observed from the XRD pattern of dolomite (Fig. S3, ESI†). The phase compositions of natural sands and dolomite were consistent with the XRF results (Tables S1 and S2, ESI†). It was reported that mechanical forces could activate $CaCO_3$ and natural serpentine to increase their reactivity by lowering the crystallinity and particle size.[38] In the XRD patterns of the precursors (Fig. 2a and b), the diffraction peaks of dolomite disappeared, because the activated dolomite reacted with the residual acid of $Al(NO_3)_3 \cdot 9H_2O$ under the mechanical force and transformed into free Ca^{2+} and Mg^{2+} or amorphous oxides. Furthermore, the crystal water of $Al(NO_3)_3 \cdot 9H_2O$ provided an micro-liquid environment for the involved reactants to completely contact with each other during grinding, while the crystal structure of Co_3O_4, ZPS and HMS was retained except for the decrease in the particle size. Thus, the diffraction peaks of Co_3O_4, ZPS and HMS were still observed in the XRD patterns of the precursors. After calcination, the typical diffraction peaks of cubic $CoAl_2O_4$ (2θ = 31.23°, 36.79°, 44.74°, 55.57°, 59.27° and 65.13°) appeared in the XRD patterns of CP-CB/ZPS-A and CP-CB/HMS-A (PDF card no. 70-0753), suggesting that Co_3O_4 successfully reacted with the Al species derived from $Al(NO_3)_3 \cdot 9H_2O$. Furthermore, the hexagonal $CaAl_2O_4$ crystal phase (2θ = 18.99°, 30.11° and 35.68°) was also found with the incorporation of dolomite due to the reaction between the Ca species derived from dolomite and Al species. Meanwhile, partial activated quartz in ZPS and HMS could react with the Al and Ca species to form anorthite;[39] and thus, the peaks of anorthite were observed in the XRD patterns of CP-D/CB/ZPS-A, CP-D/CB/HMS-A, CP-D/ZPS-A and CP-D/HMS-A, respectively. As depicted in the XRD pattern of ZPS (Fig. S2, ESI†), there was no anorthite phase except quartz. Moreover, the SiO_2 content of dolomite was only 1.303 wt%, but the typical diffraction peaks of anorthite ($CaAl_2Si_2O_8$) appeared in Pre-D/CB-HMS-A and CP-D/ZPS-A, suggesting that quartz in ZPS acted as the silicon source to form anorthite. Interestingly, the diffraction peaks of feldspar disappeared in Pre-D/CB-HMS-A, while the weak diffraction peaks of quartz were still observed after ball milling (Fig. 2b). Similarly, anorthite was also found in the XRD pattern of CP-D/CB-HMS-A, and the peak intensity of quartz became weaker, thus it suggested that both of quartz and feldspar in HMS could serve as the silicon source for the formation of anorthite.

The crystal phases in CP-D/ZPS-A and CP-D/HMS-A were assigned to spinel $MgAl_2O_4$ based on the reaction between Al and Mg species derived from dolomite. Both $MgAl_2O_4$ and $CoAl_2O_4$ possessed spinel structure, and their diffraction peaks overlapped, and thus it was not easy to distinguish them in CP-D/CB/ZPS-A and CP-D/CB/HMS-A. Consequently, the constructed composite pigments without dolomite were composed of $CoAl_2O_4$ and quartz, while the phase compositions were $CaAl_2O_4$, anorthite, $CoAl_2O_4$ and quartz in CP-D/CB/ZPS-A and CP-D/CB/HMS-A. By contrast, the components in CP-D/ZPS and CP-D/HMS consisted of $MgAl_2O_4$, $CaAl_2O_4$, anorthite and quartz.

3.3 FTIR spectra

The changes in the samples prepared at different steps could be analyzed using the FTIR spectra (Fig. 2c and d). For ZPS and HMS, the observed absorption peaks located at approximately 1085, 779, 691 and 460 cm^{-1} were ascribed to the Si–O asymmetric stretching vibration, Si–Si stretching vibration, O–Si–O and Si–O–Si bending vibration, respectively, while the peak at 1041 cm^{-1} in HMS was assigned to the Si–O symmetric stretching band.[40] The absorption peaks below 700 cm^{-1} were assigned to the M–O vibration. The asymmetric stretching, out-of-plane bending and in-plane bending modes of the carbonate groups in dolomite were located at 1438, 879 and 729 cm^{-1}, respectively. The absorption peaks at 1825 and 2532 cm^{-1} were related to the combination of the above-mentioned bending modes.[41]

After grinding, the typical absorption peaks of dolomite disappeared in the FTIR spectra of Pre-D/CB/ZPS-A and Pre-D/CB/HMS-A, suggesting that dolomite was involved in the reaction with the residual acid of hydrous $Al(NO_3)_3$. The absorption bands at around 660 and 580 cm^{-1} indicated the existence of Co_3O_4.[42] In addition, the absorption bands of ZPS and HMS vanished except for the Si–O stretching vibration, which might be due to the decrease in their relative content in the precursors. The presence of NO_3^- could be confirmed by the peaks of 1384 and 825 cm^{-1}, which were attributed to the stretching vibration and bending vibration of N–O, respectively.[43] Generally, the high-temperature crystallization is crucial to prepare the mixed metal oxide-based inorganic pigments. By contrast, the typical absorption peaks of $CoAl_2O_4$ were found at 682, 563 and 512 cm^{-1} in CB-D/CB/ZPS-A, and 679, 564 and 520 in CB-D/CB/HMS-A after calcination, respectively.[44] Moreover, the broad Si–O absorption bands centered at around 1040 cm^{-1} were related to quartz and anorthite,[39] while the weak absorption band at 1170 cm^{-1} was assigned to the vibration of Si–O non-bridge oxygen bonds in the SiO_4 tetrahedron. The weak absorption peak of 855 cm^{-1} was indicative of the existence of $CaAl_2O_4$ in CB-D/CB/ZPS-A,[45] but it was not observed in CB-D/CB/HMS-A. Thus, the compositions of the precursors and composite pigments obtained from the FTIR spectra were consistent with their XRD patterns.

3.4 TG-DTA curves

From the precursor to composite pigments, the thermal behavior of the samples was studied by TG-DTA curves. Fig. 3 presents the thermal behavior curves of dolomite, Pre-D/CB/ZPS-A and Pre-D/CB/HMS-A from 30 to 1100 °C. The weight loss of dolomite included two main steps according to the TG-DTA curves (Fig. 3a): the first endothermic process was ascribed to the formation of MgO and calcite in the temperature range of 690–810 °C, and the second mass loss was related to the decomposition of calcite between 810 and 920 °C.[46] Interestingly, the typical thermal decomposition endothermic peaks of dolomite were not observed in the precursors of Pre-D/CB/

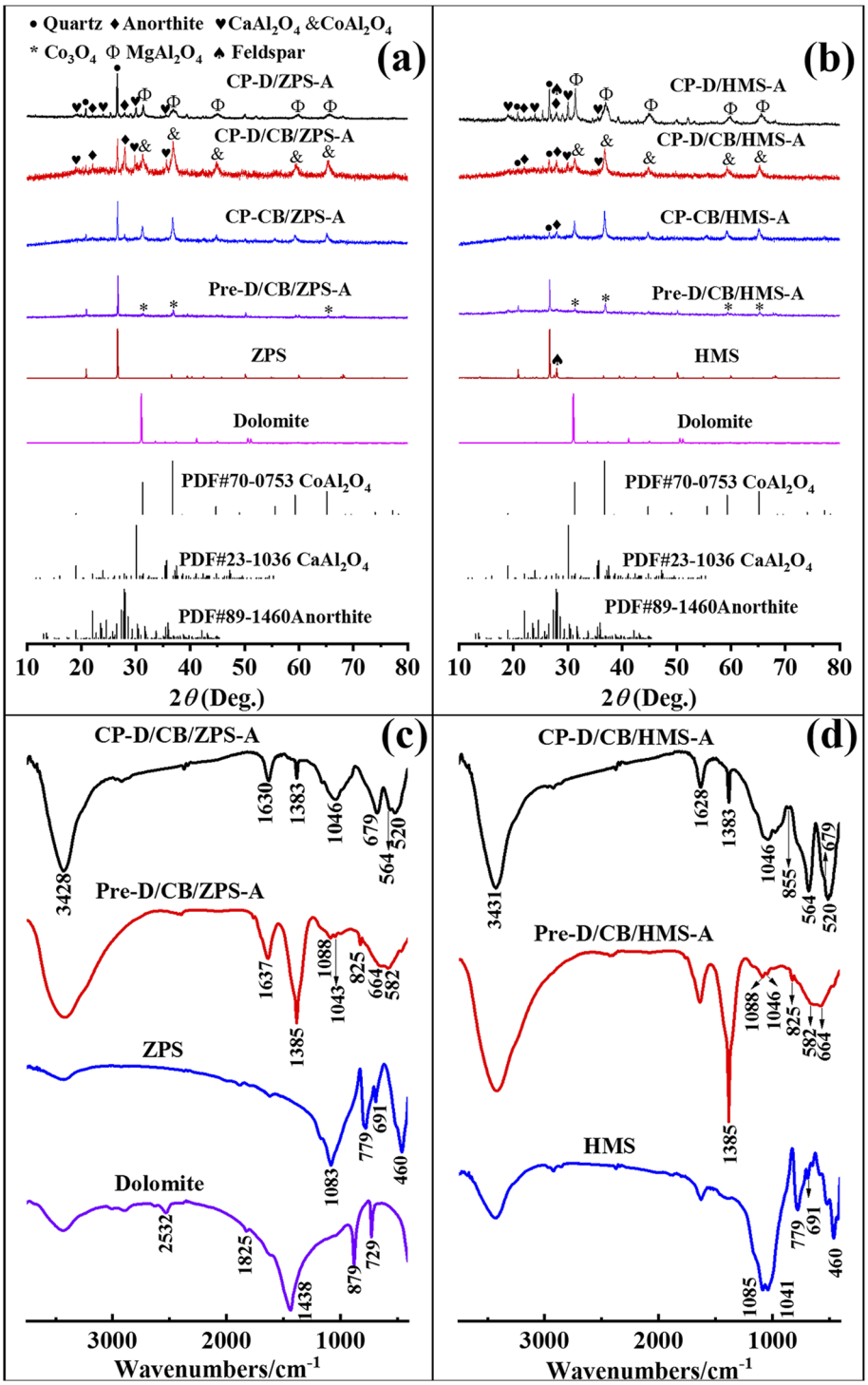

Fig. 2 XRD patterns of dolomite, ZPS-related (a) and HMS-related samples (b), FTIR spectra of (c) dolomite, ZPS, Pre-D/CB/ZPS-A and CP-D/CB/ZPS-A, (d) HMS, Pre-D/CB/HMS-A and CP-D/CB/HMS-A.

ZPS-A (Fig. 3b) and Pre-D/CB/HMS-A (Fig. 3c), indicating that dolomite might react with the residual acid from $Al(NO_3)_3 \cdot 9H_2O$. Furthermore, the whole mass loss of the precursors reached approximately 60%, and three endothermic peaks were observed during the heating process. Among them, the peak at 78 °C was ascribed to the removal of crystallization water, which was completely removed at a temperature of 112 °C. Next, the nitrogen-containing compounds began to pyrolyze, and the mass loss greatly reduced when the heating temperature was above 500 °C, involved in the transformation from Co_3O_4 to CoO as well as the high-temperature crystallization reaction with metal oxides for the generation of $CaAl_2O_4$, $MgAl_2O_4$, anorthite

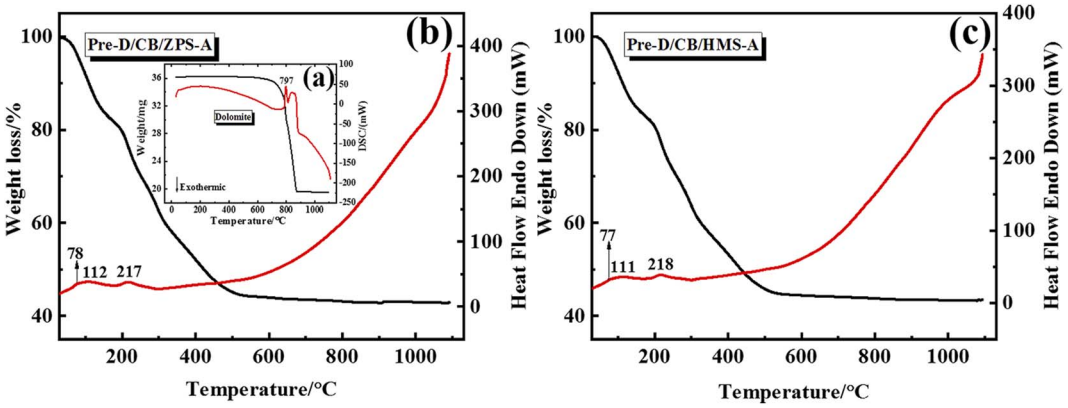

Fig. 3 TG-DTA curves of (a) dolomite, (b) Pre-D/CB/ZPS-A and (c) Pre-D/CB/HMS-A from 30 to 1100 °C.

and $CoAl_2O_4$.[39,47–49] In contrast to these two TG-DTA curves, no obvious differences were observed for the mass loss, endothermic peak location and curve trend, suggesting that the types of natural sands hardly affected the normal thermal decomposition of aluminum nitrate and the formation of the crystal phases.

3.5 XPS spectra

The binding energy and corresponding assignment of the fine XPS spectra of Pre-D/CB/ZPS-A and CP-D/CB/ZPS-A were summarized (Table S4, ESI†). From the XPS spectra of Co 2p in Fig. 4a, the low signal-to-noise ratio indicated the low content of Co element in Pre-D/CB/ZPS-A, while the improved signal-to-noise ratio of Co 2p in CP-D/CB/ZPS-A was attributed to the thermal decomposition of NO_3^- during the calcination process, which resulted in an increase in the relative content of Co element. The four weak split peaks located at 779.81 eV, 787.07 eV, 797.17 eV and 803.27 eV of Co 2p in the precursor were observed, where 779.81 eV and 797.17 eV were assigned to Co^{3+}, suggesting the existence of Co_3O_4.[50] The four typical split peaks of $CoAl_2O_4$ were located at 781.77, 786.86, 797.34 and 803.43 eV in CP-D/CB/ZPS-A. However, these four peaks shifted to higher binding energies (BE) than pure $CoAl_2O_4$ prepared in the same way at a stoichiometric ratio, which was closely related to the interaction between $CoAl_2O_4$ and formed calcium magnesium aluminates. The peak of Al 2p in the precursor at 75.06 eV was ascribed to Al_2O_3 (Fig. 4b),[51] suggesting that $Al(NO_3)_3$ was partially transformed into amorphous Al_2O_3 after the grinding process.

After the precursors were calcined, the split peak of composite pigments at 75.07 eV corresponded to $CaAl_2O_4$.[52] while the peaks at 74.44 and 73.78 eV represented 6-coordinated Al and 4-coordinated Al in $CoAl_2O_4$, respectively.[53] Similarly, the incorporation of dolomite resulted in a higher BE of Al 2p for composite pigments, which was related to the crystal distortion. In the case of Ca 2p (Fig. 4c), the two improved typical peaks at 348.42 and 352.13 eV were ascribed to $Ca(NO_3)_2$ in the precursor compared with the BE of Ca 2p in dolomite (Fig. S4a, ESI†), indicating that dolomite changed into Ca^{2+} and then combined with NO_3^- during grinding.[54] By contrast, two peaks of composite pigments at 347.69 and 348.60 eV represented Ca $2p_{3/2}$ of $CaAl_2O_4$, and the Ca $2p_{1/2}$ line was fixed at an energy separation of 3.50 eV compared with Ca $2p_{3/2}$.[55] In addition, the BE of Mg 1s in dolomite was 1304.28 eV (Fig. S4b†), but the BE of Mg 1s in the precursor (1304.11 eV) and composite pigments (1304.00 eV) obviously decreased, where the BE at 1304.11 eV in the precursor was attributed to $Mg(NO_3)_2$, while the BE at 1304 eV represented the formation of $MgAl_2O_4$ (Fig. 4d).[56] This indicated that $MgCO_3$ in dolomite transformed into Mg^{2+}, and then formed amorphous $Mg(NO_3)_2$ with NO_3^- in the precursor, and finally reacted with aluminium oxide to generate $MgAl_2O_4$ in the high-temperature crystallization process.

In the case of Si 2p, two split peaks at 103.39 and 102.14 eV were observed for ZPS-A (Fig. 4e), which corresponded to the Si–O and SiO_2 bonds, respectively, and this result was also consistent with the previous report.[57] For the obtained precursors, the peak at 102.07 eV was due to the $SiO_2 \cdot Al_2O_3$ species formed under the mechanical force, in which Al_2O_3 was derived from $Al(NO_3)_3$, and the peak at 103.07 eV was attributed to quartz. Interestingly, there were also two split BE peaks for Pre-D/CB/ZPS-A (102.07 and 103.07 eV) and CP-D/CB/ZPS-A (102.12 and 102.84 eV). Among them, the peak at 102.12 eV was assigned to the formation of the Si–O–Al chemical bond for CP-D/CB/ZPS-A, while the one at 102.84 eV was due to quartz.[58–60] This suggested that the mechanical force promoted the formation of $SiO_2 \cdot Al_2O_3$ species in the precursor, and then $CoAl_2O_4$ were bonded with ZPS *via* the Si–O–Al bond. Furthermore, the composite pigments obtained by directly calcining the precursor, NO_3^-, remained in the precursors, which was also confirmed by the N 1s high-resolution scanning spectrum in addition to the FTIR spectra. For N 1s of Pre-D/CB/ZPS-A (Fig. 4f), the BE at 407.83 and 400.13 eV was attributed to the NO_3^- and N–O-M bonds, respectively.[61] Therefore, it could be concluded that dolomite and $Al(NO_3)_3$ could react with each other during the grinding process, wherein $Al(NO_3)_3$ was transformed into Al_2O_3 while dolomite turned into $Ca(NO_3)_2$ and $Mg(NO_3)_2$, and all the produced substances were well mixed and interacted with ZPS *via* the chemical bond (Si–O–Al), which was beneficial for the growth of $CoAl_2O_4$ nanoparticles on the surface of quartz and dolomite.

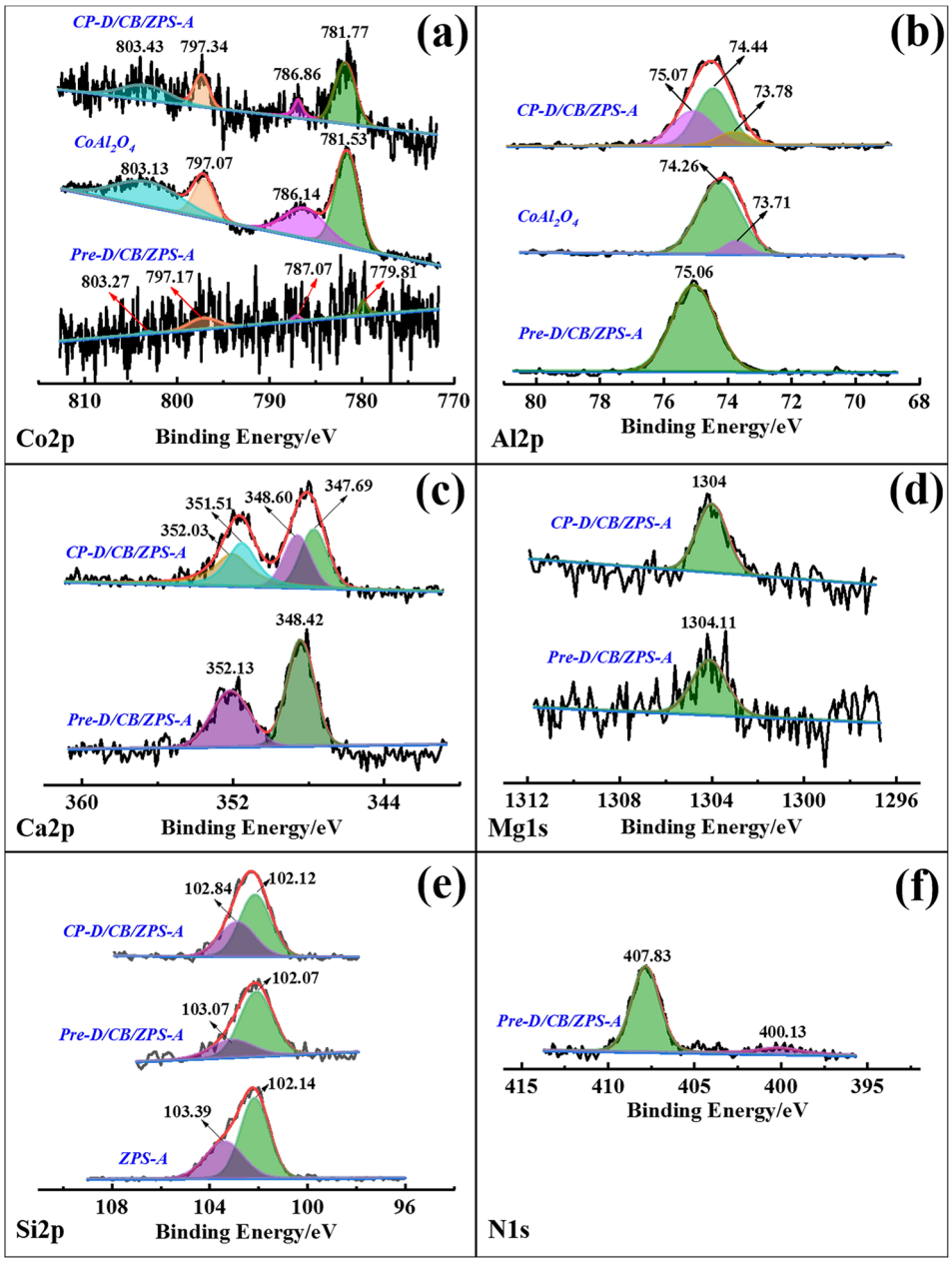

Fig. 4 XPS high-resolution scanning spectra of ZPS-A, Pre-D/CB/ZPS-A, CP-D/CB/ZPS-A and pure $CoAl_2O_4$ prepared by the same preparation process: (a) Co 2p, (b) Al 2p, (c) Ca 2p, (d) Mg 1s, (e) Si 2p and (f) N 1s.

3.6 TEM images

To investigate the effect of incorporation of dolomite on the morphology change with the assistance of the mechanical force as well as the growth and distribution of $CoAl_2O_4$ nanoparticles, the TEM images of dolomite and composite pigments are shown in Fig. 5. Obviously, pure dolomite presented a typical stacked lamellar morphology with good crystallized structure (Fig. 5a and b). After grinding with the reactants and calcination, the stacked thickness decreased under the mechanical force, but the lamellar morphology was retained (Fig. 5c). Interestingly, the irregular shaped nanoparticles with a size of about 10 nm were anchored on the surface of lamellar morphology, indicating that dolomite could be served as a promising substrate to induce the *in situ* growth of $CoAl_2O_4$ particles, which effectively prevented the aggregation of $CoAl_2O_4$ nanoparticles. Furthermore, the pores were also observed in composite pigments (Fig. 5c), which might be attributed to the acid etching during grinding. From the HR-TEM image of composite pigments (Fig. 5d), the lattice fringes were assigned to $CoAl_2O_4$, $CaAl_2O_4$, quartz and anorthite, which was also well consistent with the XRD results. This suggested that composite pigments exhibited a form of mixed phases, and the partial diffraction patterns were assigned to cubic $CoAl_2O_4$ after calibration (Fig. 5e). Consequently, the

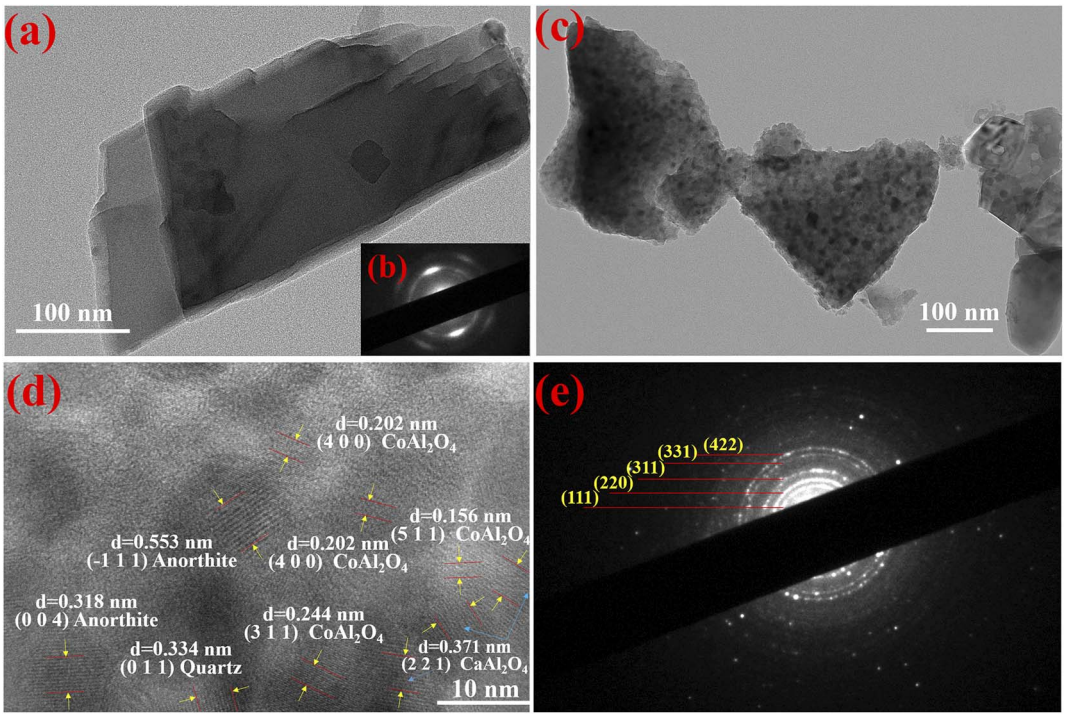

Fig. 5 TEM images of dolomite (a) and composite pigments (c). HRTEM image of composite pigments (d), SAED images of dolomite (b) and composite pigments (e).

lamellar morphology derived from dolomite was kept after grinding, and dolomite could be used as the substrate to induce the *in situ* growth of pigment nanoparticles. Moreover, dolomite also provided Ca and Mg sources to promote the formation of $CaAl_2O_4$ and $MgAl_2O_4$ to regulate the blue intensity of $CoAl_2O_4$ pigments.

3.7 Evaluation of environmental stability

Compared with the digital images of composite pigments before and after treatment with HCl, NaOH and ethanol (Fig. 6), no obvious difference in the color could be distinguished by the human eye. In fact, the color variations of the pigments are usually evaluated by ΔE^*, which is calculated according to eqn (1). Furthermore, the color saturation variations (ΔC^*) can also be used to assess the environmental stability of the as-prepared composite pigments before and after treatment, which is obtained by calculating the C^* value difference before and after treatment:

$$\Delta E^* = \sqrt{(\Delta L^*)^2 + (\Delta a^*)^2 + (\Delta b^*)^2} \quad (1)$$

After treatment with different chemical reagents, no obvious change was found in the colors of composite pigments (Fig. 6a), while the ΔE^* and ΔC^* values in HCl and ethanol were small (Fig. 6b). However, the ΔE^* and ΔC^* values after NaOH treatment were higher than those of HCl and ethanol treatment, suggesting that the composite pigments exhibited better stability in HCl and ethanol than in NaOH, which might be related to the partial dissolution of the exposed quartz in composite pigments, which resulted in a slight decrease in the L^* and b^* values. It was worth mentioning that the blueness hue of the treated composite pigments was still superior to other reports (Table S3, ESI†). Thus, the obtained composite pigments presented excellent environmental stability.

3.8 Possible coloring mechanisms of composite pigments

Generally, the d or f orbitals of the transition metal ions can be split into orbits with different energy levels in different crystal fields. The electrons will selectively absorb and reflect visible light with different wavelengths transitioning from low to high energy levels according to the energy level difference, while the superposition of reflective visible light is the color observed by the human eye, which is also the coloration mechanism for transition metals. For $CoAl_2O_4$, the source of color is assigned to the intense allowed transitions (AT) and weak forbidden spin transitions (FST) of 4-coordinated Co^{2+} electrons, which are located at absorption bands of about 554, 584 and 622 nm as well as 480 and 408 nm, respectively.[62] That is to say, $CoAl_2O_4$ mainly absorbs nonblue light in the AT and little blue light in the FST (reflected by blue light).

Fig. 7a presents the reflectance spectra of the samples. The absorption bands related to AT had no obvious change, while the absorption bands of FST were obviously improved with the introduction of dolomite. This indicated that composite pigments prepared with dolomite reflected more blue visible light than those composite pigments without dolomite, which was also a direct evidence to explain why the color performance of D/CB/ZPS and D/CB/HMS was better than that of CB/ZPS and CB/HMS, respectively.

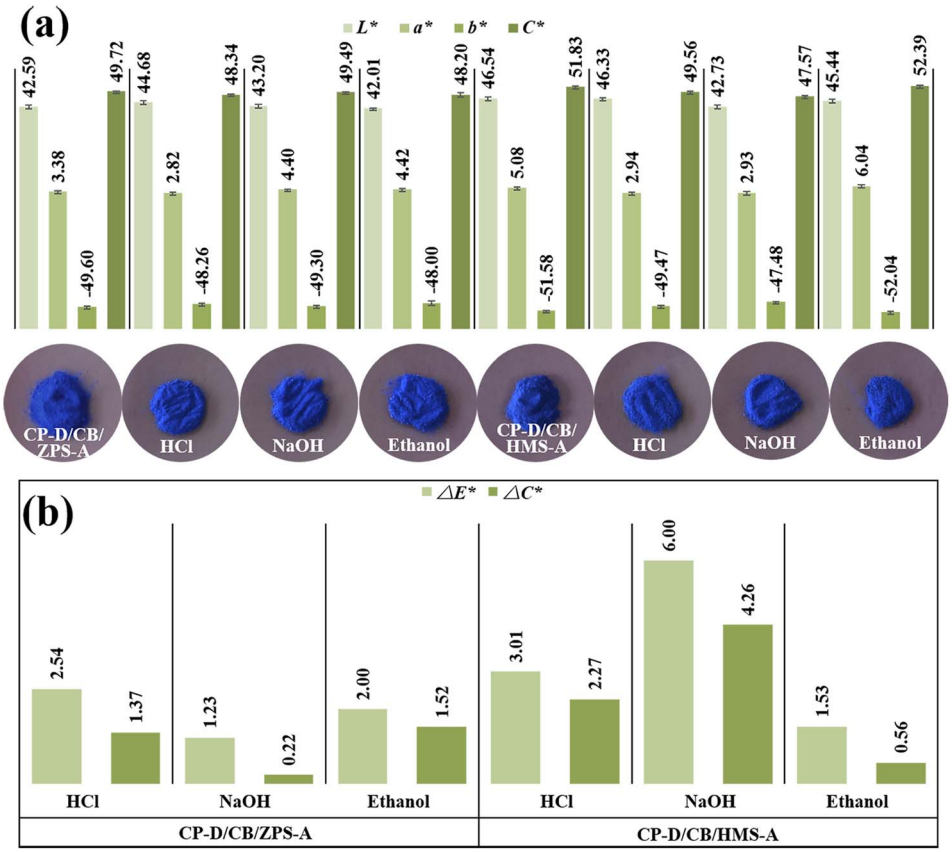

Fig. 6 (a) Chroma values and digital photos, (b) ΔE^* and ΔC^* values of composite pigments before and after treatment with chemical reagents.

Recently, Zhai *et al.* have reported that oxygen vacancies were fundamental defects in pure $CaAl_2O_4$ nanocrystals, which could serve as the source of the blue emission.[63,64] Because of the coexistence of $CaAl_2O_4$ and $CoAl_2O_4$ in the composite pigments, the outermost electrons of 4-coordinated Co^{2+} could transit to the oxygen vacancy of $CaAl_2O_4$ and then be captured except for the transition to the split energy level of cobalt. Next, the captured electrons could radiatively recombine with the low-energy calcium vacancy and emit photons with an energy of 2.88 eV (430.6 nm) to produce blue emissions. Therefore, the reflectance to blue light was strengthened for CP-D/CB/ZPS-A and CP-D/CB/HMS-A (Fig. 7a), which was also the fundamental reason why the color performance was greatly improved after the incorporation of dolomite.[21] Furthermore, this study also provided a new clue that $CoAl_2O_4$ exhibited better color performance after the incorporation of Ca^{2+}. According to our previous study, both $MgAl_2O_4$ and $CoAl_2O_4$ were cubic spinel-structure phases, and the ionic radii of 4-coordinated Mg^{2+} (0.57 Å) and Co^{2+} (0.56 Å) were almost the same. Thus, Mg^{2+} could occupy the tetrahedral Co^{2+} sites of $CoAl_2O_4$ to form

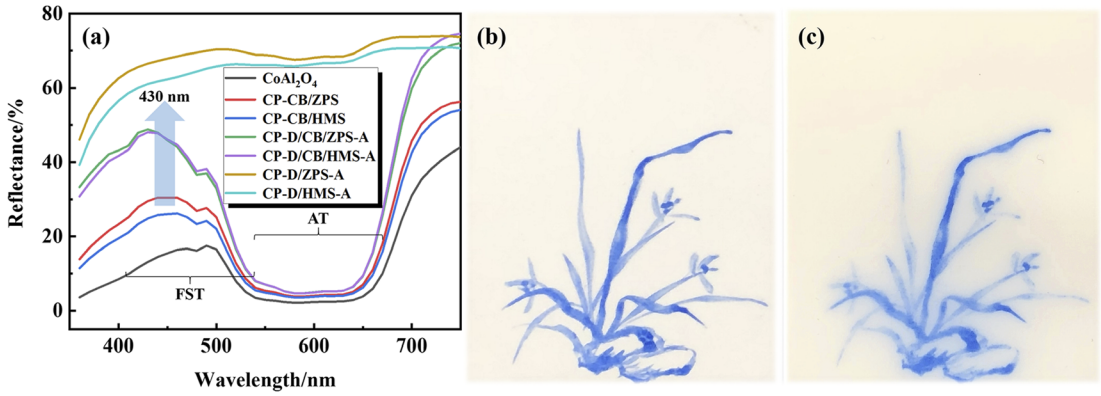

Fig. 7 Reflectance spectra of $CoAl_2O_4$, CP-CB/ZPS, CP-CB/HMS, CP-D/CB/ZPS, CP-D/CB/HMS, CP-D/ZPS and CP-CB/HMS (a), digital images of the orchid drawn on the Al_2O_3 substrate (b) before and (c) after calcination.

a $MgAl_2O_4$–$CoAl_2O_4$ solid solution during the high-temperature crystallization process, which influenced the outermost electronic transition by distorting the crystal structure, and further changed the coloring degree of $CoAl_2O_4$ pigments.[20] Based on the above-mentioned analysis and discussion, the generated $CoAl_2O_4$ nanoparticles were uniformly loaded on the dolomite surface, which effectively improved the agglomeration phenomenon of $CoAl_2O_4$ nanoparticles and the reflection to blue light. In addition, the color performance of the as-prepared composite pigments was also obviously improved after the introduction of ZPS and HMS. In fact, the $CoAl_2O_4$ nanoparticles were also dispersed on the surface of natural sands, and the agglomeration degree could be further enhanced in the presence of the natural sand substrate.[18] Finally, the substrate roles of the natural sands and dolomite might contribute to the transition process of the electrons of Co^{2+} to the oxygen vacancy of $CaAl_2O_4$, which further improved the reflectance of composite pigments to blue visible light. All of these factors synergistically enhanced the color performance of composite pigments.

3.9 Application as high-temperature ceramic pigments

For investigating the application of the obtained composite pigments as the ceramic pigment, CP-D/CB/ZPS was first ground for 4 h in a water medium, and then, moderate amounts of polyethylene glycol-800, CTAB, ethanol and polyacrylamide were dissolved in the above-mentioned pigment solution. The obtained blue ink was used to draw orchid on an Al_2O_3 substrate after magnetically stirring for 48 h. As shown in Fig. 7b, the blue ink presents a benign blue intensity and has no agglomeration or diffusion on the Al_2O_3 substrate. After calcination at 1200 °C for 2 h, the composite pigments have no agglomeration, and the blue intensity has no obvious decrease (Fig. 7c). However, the composite pigments showed some diffusion phenomenon, which might be due to the formation of an Al_2O_3–$CoAl_2O_4$ solid solution during the calcination process.[23] Therefore, the prepared composite pigments presented benign application prospects as high-temperature ceramic pigments.

4 Conclusions

Low-cost and high-performance $CoAl_2O_4$ composite pigments with high-chroma and low cobalt consumption were facilely fabricated by a dolomite-induced mechanochemical method followed by a high-temperature crystallization process. During grinding, the involved dolomite was effectively activated by mechanical forces to provide Ca^{2+} and Mg^{2+} for the formation of $CaAl_2O_4$ and $MgAl_2O_4$ accompanied by $CoAl_2O_4$ in the following calcination process. The lamellar dolomite was employed as a benign substrate for loading $CoAl_2O_4$ nanoparticles to improve their dispersion. The excellent color performance of composite pigments benefited from the substrate roles of natural sands and dolomite, intrinsic oxygen vacancy of $CaAl_2O_4$ and Mg^{2+} doping of $CoAl_2O_4$. In addition, the natural sand provided the silicon source for the formation of the anorthite to improve the lightness of composite pigments. The b^* values of the obtained composite pigments using original ZPS and HMS reached −48.12 and −45.69, respectively, which were superior to that of most cobalt-based blue pigments. In addition, the composite pigments exhibited excellent environmental stability and high temperature resistance. Therefore, this study is expected to provide a cleaner strategy for the preparation of high-performance $CoAl_2O_4$ pigments with a low cobalt content without discharging waste liquids. Furthermore, this study also provides a feasible and promising strategy for the value-added and sustainable utilization of sea sand and desert sand.

Author contributions

Hao Yang: investigation, data curation, formal analysis, writing – original draft. Bin Mu: conceptualization, investigation, methodology, writing – original draft, writing – review & editing, funding acquisition, project administration. Tenghe Zhang: investigation, data curation. Yushen Lu: investigation, formal analysis. Aiqin Wang: conceptualization, investigation, supervision, writing – review & editing, funding acquisition, project administration.

Conflicts of interest

The authors declare no conflict of interest.

Acknowledgements

This work is supported by the Science and Technology Project of the Open Competition Mechanism to Select the Best Candidates of Gansu Province, China (21ZD2JA002), and the Young Scholar of Regional Development of the Chinese Academy of Sciences (The Science Development Talent Teach words [2022] No. 10).

References

1 T. Kobayashi and L. Nakajima, *Curr. Opin. Green Sustainable Chem.*, 2021, **28**, 100439.
2 K. J. Ardila-Fierro and J. G. Hernandez, *ChemSusChem*, 2021, **14**, 2145–2162.
3 S. Iravani, *RSC Sustainability*, 2023, **1**, 72–82.
4 J. P. Lange, *ChemSusChem*, 2009, **2**, 587–592.
5 M. Leonardi, M. Villacampa and J. C. Menéndez, *Chem. Sci.*, 2018, **9**, 2042–2064.
6 D. Tan and F. Garcia, *Chem. Soc. Rev.*, 2019, **48**, 2274–2292.
7 E. Colacino, V. Isoni, D. Crawford and F. Garcia, *Trends Chem.*, 2021, **3**, 335–339.
8 T. Friscic, C. Mottillo and H. M. Titi, *Angew. Chem., Int. Ed.*, 2020, **59**, 1018–1029.
9 J. K. Awalt, P. J. Scammells and R. D. Singer, *ACS Sustainable Chem. Eng.*, 2018, **6**, 10052–10057.
10 O. Galant, G. Cerfeda, A. S. McCalmont, S. L. James, A. Porcheddu, F. Delogu, D. E. Crawford, E. Colacino and S. Spatari, *ACS Sustainable Chem. Eng.*, 2022, **10**, 1430–1439.

11 V. K. Singh, A. Chamberlain-Clay, H. C. Ong, F. Leon, G. Hum, M. Y. Par, P. Daley-Dee and F. Garcia, *ACS Sustainable Chem. Eng.*, 2021, **9**, 1152–1160.
12 F. Leon, C. F. Li, J. F. Reynes, V. K. Singh, X. Lian, H. C. Ong, G. Hum, H. D. Sun and F. Garcia, *Faraday Discuss.*, 2022, **24**, 63–78.
13 D. F. L. Horsth, J. O. Primo, N. Balaba, F. J. Anaissi and C. Bittencourt, *RSC Sustainability*, 2023, **1**, 159–166.
14 B. A. Duell, J. Li and M. A. Subramanian, *ACS Omega*, 2019, **4**, 22114–22118.
15 Z. Y. Chen, L. G. Zhang and Z. M. Xu, *J. Cleaner Prod.*, 2020, **275**, 122841.
16 X. M. He, W. J. Zhu, X. Z. Wang, F. Wang, H. Liu and Z. H. Lei, *J. Mater. Sci.*, 2020, **55**, 13569–13577.
17 W. J. Liu, T. Du, Q. X. Ru, S. X. Zuo, X. Y. Yang, C. Yao and Y. Kong, *Appl. Clay Sci.*, 2018, **153**, 239–245.
18 X. M. He, F. Wang, H. Liu, L. J. Niu and X. Wang, *J. Am. Ceram. Soc.*, 2018, **101**, 2578–2588.
19 S. Hosseini and E. Ghasemi, *Appl. Clay Sci.*, 2020, **193**, 10567.
20 H. Yang, B. Mu, Q. Wang, J. Xu and A. Q. Wang, *Ceram. Int.*, 2021, **47**, 13806–13813.
21 H. Yang, B. Mu, S. Li, X. W. Wang and A. Q. Wang, *Mater. Chem. Phys.*, 2022, **276**, 125413.
22 L. K. C. d. Souza, J. R. Zamian, G. N. d. Rocha, L. E. B. Soledade, I. M. G. d. Santos, A. G. Souza, T. Scheller, R. S. Angelica and C. E. F. d. Costa, *Dyes Pigm.*, 2009, **81**, 187–192.
23 H. Yang, B. Mu, S. Li and A. Q. Wang, *ACS Sustainable Chem. Eng.*, 2022, **10**, 9553–9564.
24 H. Yang, B. Mu, J. Xu, Y. J. Zhu and A. Q. Wang, *Ceram. Int.*, 2022, **48**, 27182–27191.
25 N. Mao, C. Zhou, J. Keeling, S. Fiore, H. Zhang, L. Chen, G. Jin, T. Zhu, D. Tong and W. Yu, *Appl. Clay Sci.*, 2018, **159**, 25–36.
26 K. Hosni and E. Srasra, *Appl. Clay Sci.*, 2009, **43**, 415–419.
27 C. H. Zhou, S. T. Xia, S. Komarneni, F. B. Kabwe, G. C. Jin and M. Q. Chu, *J. Porous Mater.*, 2019, **27**, 503–513.
28 N. Azri, R. Irmawati, U. I. Nda-Umar, M. I. Saiman and Y. H. Taufiq-Yap, *Arabian J. Chem.*, 2021, **14**, 103047.
29 T. T. Xu, X. Wang, B. Xiao and W. Liu, *Chem. Eng. J.*, 2021, **425**, 131522.
30 A. Gallo-Cordova, A. Espinosa, A. Serrano, L. Gutierrez, N. Menendez, M. D. Morales and E. Mazario, *Mater. Chem. Front.*, 2020, **4**, 3063–3073.
31 A. Tuncuk and A. Akcil, *Miner. Process. Extr. Metall. Rev.*, 2014, **35**, 217–228.
32 F. Veglio, B. Passariello and C. Abbruzzese, *Ind. Eng. Chem. Res.*, 1999, **38**, 4443–4448.
33 J. Roque-Rosell, A. Pinto, C. Marini, J. P. Burgos, J. Groenen, M. Campeny and P. Sciau, *Ceram. Int.*, 2021, **47**, 2715–2724.
34 M. H. Hamzah, S. Eavani and E. Rafiee, *Mater. Chem. Phys.*, 2020, **242**, 122495.
35 R. Chueachot and R. Nakhowong, *Mater. Lett.*, 2020, **259**, 126904.
36 A. A. Ali, E. E. Fadaly and I. S. Ahmed, *Dyes Pigm.*, 2018, **158**, 451–462.
37 Q. K. Wang, Y. Q. Wang, K. Liu, J. L. Liu, C. Wang, Y. Wang and Q. B. Chang, *Adv. Powder Technol.*, 2020, **31**, 1290–1301.
38 X. W. Li, Z. W. Lei, J. Qu, H. M. Hu and Q. W. Zhang, *Sep. Purif. Technol.*, 2017, **172**, 107–112.
39 D. P. Mukherjee and S. K. Das, *Ceram. Int.*, 2013, **39**, 571–578.
40 J. Tokarsky, V. Matejka, L. Neuwirthova, J. Vontorova, K. Mamulova Kutlakova, J. Kukutschova and P. A Capkova, *Chem. Eng. J.*, 2013, **222**, 488–497.
41 L. M. Correia, N. D. Campelo, D. S. Novaes, C. L. Cavalcante, J. A. Cecilia, E. Rodriguez-Castellon and R. S. Vieira, *Chem. Eng. J.*, 2015, **269**, 35–43.
42 Y. C. Chen, Y. G. Zhang and S. Q. Fu, *Mater. Lett.*, 2007, **61**, 701–705.
43 S. L. Wang and P. C. Wang, *Colloids Surf., A*, 2007, **292**, 131–138.
44 I. Mindru, G. Marinescu, D. Gingasu, L. Patron, C. Ghica and M. Giurginca, *Mater. Chem. Phys.*, 2010, **122**, 491–497.
45 X. L. Pan, J. L. Liu, D. Zhang and H. Y. Yu, *Ceram. Int.*, 2020, **46**, 16583–16589.
46 M. V. Kokand and W. Smykatz-Kloss, *J. Therm. Anal. Calorim.*, 2008, **91**, 565–568.
47 A. J. Zhang, B. Mu, X. W. Wang, L. X. Wen and A. Q. Wang, *Front. Chem.*, 2018, **6**, 125.
48 C. K. Chang, L. Jiang, D. L. Mao and W. J. Ying, *Mater. Chem. Phys.*, 2006, **98**, 509–513.
49 B. Liu, C. C. Hu, Y. H. Huang, H. B. Bafrooei and K. X. Song, *J. Alloys Compd.*, 2019, **791**, 1033–1037.
50 B. B. Guo, R. G. Ma, Z. C. Li, J. Luo, M. H. Yang and J. C. Wang, *Mater. Chem. Front.*, 2020, **4**, 1390–1396.
51 Y. C. Kim, H. H. Park, J. S. Chun and W. J. Lee, *Thin Solid Films*, 1994, **237**, 57–65.
52 O. O. Popoola and W. M. Kriven, *J. Mater. Res.*, 1992, **7**, 1545–1552.
53 X. L. Duan, M. Pan, F. P. Yu and D. R. Yuan, *J. Alloys Compd.*, 2011, **509**, 1079–1083.
54 B. Demri and D. Muster, *J. Mater. Process. Technol.*, 1995, **55**, 311–314.
55 L. Kalina, J. Masilko, J. Koplik and F. Soukal, *Cem. Concr. Res.*, 2014, **66**, 110–114.
56 W. Q. Wang, Y. G. Zhu, S. Q. Zhang, J. Deng, Y. Huang and W. Yan, *Minerals*, 2017, **7**, 134.
57 C. S. Patil, A. N. Kadam, D. B. Gunjal, V. M. Naik, S. W. Lee, G. B. Kolekar and A. H. Gore, *Sep. Purif. Technol.*, 2020, **247**, 116997.
58 Q. F. Wang, G. T. Ye, C. Y. Zhang, L. L. Zhu, X. J. Song and J. Ma, *J. Mater. Sci.*, 2014, **49**, 3331–3336.
59 A. Ayame and T. Kitagawa, *Bunseki Kagaku*, 1991, **40**, 673–678.
60 H. Seyama, D. Wang and M. Soma, *Surf. Interface Anal.*, 2004, **36**, 609–612.
61 K. R. Reyes-Gil, Y. P. Sun, E. Reyes-Garcia and D. Raftery, *J. Phys. Chem. C*, 2009, **113**, 12558–12570.
62 W. Zheng and J. Zou, *RSC Adv.*, 2015, **5**, 87932–87939.
63 B. G. Zhai, H. F. Xu, F. L. Zhuo and Y. M. Huang, *J. Alloys Compd.*, 2020, **821**, 153563.
64 B. G. Zhai and Y. M. Huang, *Europhys. Lett.*, 2019, **127**, 17001.